Role of silicon in accelerating the nucleation of Al₃(Sc,Zr) precipitates in dilute Al–Sc–Zr alloys

C. Booth-Morrison [a], Z. Mao [a], M. Diaz [a], D.C. Dunand [a], C. Wolverton [a],
D.N. Seidman [a,b,*]

[a] *Department of Materials Science and Engineering, Northwestern University, Evanston, IL 60208, USA*
[b] *Northwestern University Center for Atom-Probe Tomography (NUCAPT), Evanston, IL 60208, USA*

Abstract

The effects of adding 0.02 or 0.06 at.% Si to Al–0.06Sc–0.06Zr (at.%) are studied to determine the impact of Si on accelerating Al₃(Sc,Zr) precipitation kinetics in dilute Al–Sc-based alloys. Precipitation in the 0.06 at.% Si alloy, measured by microhardness and atom-probe tomography (APT), is accelerated for aging times <4 h at 275 and 300 °C, compared with the 0.02 at.% Si alloy. Experimental partial radial distribution functions of the α-Al matrix of the high-Si alloy reveal considerable Si–Sc clustering, which is attributed to attractive Si–Sc binding energies at the first and second nearest-neighbor distances, as confirmed by first-principles calculations. Calculations also indicate that Si–Sc binding decreases both the vacancy formation energy near Sc and the Sc migration energy in Al. APT further demonstrates that Si partitions preferentially to the Sc-enriched core rather than the Zr-enriched shell in the core/shell Al₃(Sc,Zr) (L1₂) precipitates in the high-Si alloy subjected to double aging (8 h/300 °C for Sc precipitation and 32 days/400 °C for Zr precipitation). Calculations of the driving force for Si partitioning confirm that: (i) Si partitions preferentially to the Al₃(Sc,Zr) (L1₂) precipitates, occupying the Al sublattice site; (ii) Si increases the driving force for the precipitation of Al₃Sc; and (iii) Si partitions preferentially to Al₃Sc (L1₂) rather than Al₃Zr (L1₂).

© 2012 Acta Materialia Inc. Published by Elsevier Ltd. All rights reserved.

Keywords: Aluminum alloys; Precipitation kinetics; Scandium; Zirconium; Silicon

1. Introduction

Upon aging, supersaturated Al–Sc alloys form coherent nanoscale L1₂-ordered Al₃Sc precipitates, which provide significant strengthening to ~300 °C [1–7]. The industrial applicability of Al–Sc alloys is limited, however, by the cost of Sc, motivating the replacement of as much Sc as possible with other solute elements, such as Mg, Ti, Hf, Zr and rare-earth (RE) elements [3,7–10]. The addition of Zr has proved particularly effective for improving coarsening resistance due to the formation of Al₃(Sc$_x$Zr$_{1-x}$) (L1₂) precipitates, which consist of a Sc-enriched core surrounded by a Zr-enriched shell [3,11–17]. The addition of ~0.025 at.% Si to dilute Al–Sc alloys with Sc concentrations of 0.06 at.% and lower was shown by Beeri et al. to increase alloy microhardness significantly [18]. This strength improvement is industrially relevant, because Si is a common impurity in Al and would reduce the amount of expensive Sc needed to achieve a given strength. Silicon has been shown to accelerate precipitation in aluminum alloys containing various transition metals, such as Al–Ti–Si [19], Al–Hf–Si [20,21], Al–Cu–Si [22,23] and Al–Zr–Si [24–26].

The Al–Sc–Si phase diagram is not well understood, though the relevant research is reviewed in Ref. [10]. The isothermal Al–Sc–Si phase diagram at 500 °C is presented, based on work from Tyvanchuk et al. [27], and the solubility of Sc in α-Al is reported to be constant with increasing Si concentration, while the solubility of Si is reduced

slightly with increasing Sc concentration [10]. Based on this phase diagram, changes in solute solubility are unlikely to be responsible for the increased microhardness due to the dilute addition of Si observed by Beeri et al. The addition of Si to Al–Sc was shown to result in discontinuous precipitation of coarse coherent Al_3Sc precipitates during post-solidification cooling [28–30], and the formation of a tetragonal Sc_2AlSi_2 intermetallic compound, the V-phase, in a study of alloys with 0.24 at.% Sc and Si concentrations ranging from 0 to 0.8 at.% [31–34]. These processes deprive the Al matrix of Sc, decreasing the volume fraction of strengthening nanoscale Al_3Sc precipitates, and are avoided by limiting the Si concentration to <0.08 at.% in very pure Al–Sc alloys [31,33]. Studies of Al–0.24 at.% Sc alloys with Si concentrations ranging from 0 to 0.8 at.% revealed an increase in the as-cast microhardness with increasing Si content, owing to an increase in the amount of discontinuous and/or continuous precipitation of Al_3Sc [30,33] during post-solidification cooling. The peak microhardness of these alloys after heat treatment at temperatures ranging from 250 to 350 °C decreased slightly with increasing Si concentration, while the Si-containing alloys [30] had a peak microhardness that was ~20% smaller than the microhardness of the Si-free alloy [28–30]. The decreases in peak strength with increasing Si concentration was attributed to the discontinuous precipitation of coarse Al_3Sc and the V-phase, limiting the amount of Sc available for forming nanoscale Al_3Sc precipitates during subsequent aging.

The addition of ~0.025 at.% Si to Al–Sc alloys with Sc concentrations <0.06 at.% was shown to increase the resulting alloy microhardness significantly, a result that was suggested to be due to an acceleration in the Al_3Sc ($L1_2$) precipitation kinetics [18]. The detailed reasons for this acceleration were initially unclear. Recent research, however, combining atom-probe tomography (APT) and first-principles calculations on Al–0.1Sc–0.05Si (at.%) aged at 300 °C showed a significant energetic driving force for the partitioning of Si from the matrix to the Al sublattice of Al_3Sc, resulting in a larger chemical driving force for precipitation [35]. It was suggested that the increased precipitation kinetics may have been due to an attractive binding energy between Si and vacancies [36,37], which would lead to the formation of Si–vacancy clusters and provide nuclei for heterogeneous nucleation [35]. Another explanation for the accelerated precipitation was that the incorporation of Si in Al_3Sc decreases the α-Al (face-centered cubic (fcc))/$(AlSi)_3Sc$ ($L1_2$) precipitate interfacial free energy, decreasing the net reversible work to create a nucleus of critical radius.

To clarify the role of Si in the precipitation of Al_3Sc in dilute Al–Sc alloys, the effects of adding 0.02 or 0.06 at.% Si on alloy strength and precipitate evolution of Al–0.06Sc–0.06Zr (at.%) are studied herein by microhardness and APT. The Al–0.06Sc–0.06Zr (at.%) alloy was identified as offering both coarsening and creep resistance up to 400 °C, making this alloy an ideal candidate for low-stress,

high-temperature transportation applications [38–40]. The experimental results are complemented with first-principles calculations to shed light on the atomistic mechanisms that accelerate the nucleation of Al_3Sc precipitates due to Si additions. Previous first-principles calculations have been performed on Al–Sc, Al–Zr and Al–Si alloys, which form the basis of the Al–Zr–Sc–Si system [14,41–49]. Additionally, the solute vacancy binding energies and activation energies for diffusion of Zr, Sc and Si in Al have been calculated [36,37,50,51]. Building on these calculations, the solute–solute binding energies of Si, Sc and Zr in Al, and the Sc migration energy in Al, with and without Si are calculated. Then, the partitioning and site substitution of Si across the Al (fcc)/$Al_3Sc(L1_2)$ interface are assessed. From this research, the role of Si on accelerating the diffusion of Sc in Al, and consequently the nucleation of Al_3Sc precipitates, is elucidated.

2. Experimental procedures and computational methodology

2.1. Alloy compositions and processing

Two quaternary alloys with nominal compositions of Al–0.06Zr–0.06Sc–0.06Si and Al–0.06Zr–0.06Sc–0.02Si (at.%) (Al–0.2Zr–0.1Sc–0.06Si and Al–0.2Zr–0.1Sc–0.02Si (wt.%)) were cast; hereafter, they are denoted as the high-Si and low-Si alloys, respectively. Their compositions in the as-cast state are presented in Table 1, as measured by direct current plasma emission spectroscopy (DCPMS) (ATI Wah Chang, Albany, OR). The Fe concentration of the alloys determined by DCPMS was 0.0065 at.%. The alloys were inductively melted to a temperature of 900 °C and cast from 99.99 at.% pure Al, pure Si and Al–0.96 at.% Sc, Al–3 at.% Zr and Al–78 at.% Er master alloys. The alloys were cast into a graphite mold placed on a copper platen to encourage directional solidification and discourage the formation of shrinkage cavities. The castings were homogenized in air at 640 °C for 72 h and then water quenched to ambient temperature. Two separate aging studies were conducted: (i) isothermal aging at 275 or 300 °C for times ranging from 0.5 to 24 h; and (ii) two-stage isothermal aging consisting of a first heat-treatment at 300 °C for 8 h followed by aging at 400 °C for 32 days. A two-stage heat treatment was determined to provide optimal strengthening in Al–0.06Sc–0.06Zr (at.%) [39]. The first aging at 300 °C provides peak strengthening from Al_3Sc precipitates, while the second aging at 400 °C allows for the precipitation of the Zr-enriched shell, which renders the resulting core/shell $Al_3(Sc,Zr)$ precipitates coarsening resistant [39]. These aging temperatures were determined in the absence of Si.

2.2. Analytical techniques

Precipitation in these alloys was monitored by Vickers microhardness performed on a Duramin-5 hardness tester (Struers) using a 200 g load applied for 5 s on samples

Table 1
Compositions of the two alloys investigated (at.%), as measured by DCPMS and LEAP tomography; measurement uncertainty is given in parenthesis after the significant digit to which it applies.

Nominal alloy composition	Heat treatment	Measured alloy composition (DCPMS)			Measured alloy composition (LEAP tomography)		
		Zr	Sc	Si	Zr	Sc	$Si^{2+,a}$
Al–0.06Zr–0.06Sc–0.06Si	1 h/300 °C	0.068(1)	0.060(1)	0.060(1)	0.0475(4)	0.0507(4)	0.0629(4)
	8 h/300 °C + 32 days/400 °C				0.0501(4)	0.0515(4)	0.0341(3)
Al–0.06Zr–0.06Sc–0.02Si	1 h/300 °C	0.059(1)	0.066(1)	0.018(1)	0.0532(3)	0.0565(5)	0.0204(3)
	8 h/300 °C + 32 days/400 °C				0.0450(2)	0.0654(3)	0.0126(1)

[a] The reported Si concentrations are inaccurate, owing to difficulties in quantifying Si in Al using LEAP tomography (Section 2.2).

polished to a 1 µm surface finish. Fifteen indentations were made per specimen across several grains.

Specimens for three-dimensional (3-D) local-electrode atom-probe (LEAP) tomography were prepared by cutting blanks with a diamond saw to dimensions of $\sim 0.35 \times 0.35 \times 10$ mm^3. These were electropolished at 8–20 V DC using a solution of 10% perchloric acid in acetic acid, followed by a solution of 2% perchloric acid in butoxyethanol at room temperature. Pulsed-laser APT was performed using a LEAP 4000× Si tomograph (Cameca Atom-Probe Technology Center, Madison, WI) [52–58] at a specimen temperature of 35 K, employing focused picosecond ultraviolet (UV) laser pulses (wavelength = 355 nm) with a laser beam waist of <5 mm at the e^{-2} diameter. A UV laser energy of 0.075 nJ pulse^{-1}, a pulse repetition rate of 250 kHz, and an evaporation rate of 0.04 ions pulse^{-1} were employed. LEAP tomographic data were analyzed with the IVAS 3.4.1 program (Cameca Instruments). The precipitate/matrix heterophase interfaces were delineated with Sc isoconcentration surfaces, and the compositional profiles across the matrix/precipitate interface were obtained with the proximity histogram methodology [59,60]. Given the difficulties of determining the location of the matrix/precipitate interface for these dilute alloys, the precipitate volume fractions, radii and compositions were obtained using a modified envelope method [61], as used in previous studies of dilute Al–Sc alloys [62–66]. The measurement errors for all quantities were calculated based on counting statistics and standard error propagation techniques [67].

Previous attempts to measure Si concentrations in Al by LEAP tomography resulted in measured values that are smaller than both the expected nominal value and the value measured by DCPMS [18,66]. LEAP tomography measured Si concentrations in a study of Al–Sc–Li–Yb–Si alloys [66] were shown to be incorrect due to an artifact in the spatial detection of Si, which segregates at low-index crystallographic poles caused by surface migration of the Si atoms during pulsed laser evaporation. The Si atoms are then preferentially retained with respect to Al until the atomic terraces evaporate completely. For the LEAP tomograph operating conditions employed herein, which were the same as those used previously [66], Si evaporates exclusively as $^{28}Si^{2+}$, whose peak in the mass spectrum lies in the decay tail of the $^{27}Al^{2+}$ peak, further reducing the accuracy of the concentration measurement. As before

[66], the $^{28}Si^{2+}$ concentration is reported. Table 1 shows that the LEAP tomograph measured $^{28}Si^{2+}$ concentrations of the alloys aged 1 h at 300 °C are in good agreement with the nominal and DCPMS measured values. The LEAP tomograph measured $^{28}Si^{2+}$ concentrations for the alloys following two-stage aging differ significantly, however, from the nominal and DCPMS values, evidence that the Si detection issues referenced are microtip-specific, depending on tip morphology and specific low-index $h\,k\,l$ poles in an analyzed specimen.

The effect of Si on nucleation kinetics is studied, employing the partial radial distribution function (RDF) technique applied to LEAP tomographic data, which provides a measure of solute–solute clustering [68,69]. A partial RDF at a radial distance r is defined as the average concentration distribution of component i around a given solute species X, $\langle C_i^X(r) \rangle$, normalized to the overall concentration of i atoms c_i^0, in the sampled volume:

$$\text{Partial RDF} = \frac{\langle c_i^X(r) \rangle}{c_i^0} = \frac{1}{c_i^0} \sum_{k=1}^{N_X} \frac{N_j^k(r)}{N_{tot}^k(r)} \quad (1)$$

where $N_i^k(r)$ is the number of i atoms in a radial shell around the kth X atom that is at the center of a shell with radius r, $N_{tot}^k(r)$ is the total number of atoms in this shell, and N_X is the number of X atoms in the analyzed volume. The average concentration distributions around a solute species are measured in 0.5-Å-thick shells, and only the partial RDF for $r > 2.5$ Å are presented herein, because physical interpretation at smaller r values is difficult, owing to possible ion trajectory effects during LEAP analyses. Partial RDF values of unity describe perfectly random distributions, and partial RDF values greater than unity describe clustering of the species i and X. To minimize the impact of the Si detection issues, the partial RDF technique is applied only to the samples aged 1 h at 300 °C, whose $^{28}Si^{2+}$ concentrations are in agreement with the DCPMS measured values. Additionally, regions of the matrix that were free of low-index poles were selected for partial RDF analysis in the two samples, to avoid artificially high concentrations of Si, as noted.

2.3. Computational methodology

The density functional theory (DFT) $T = 0$ K calculations employ the plane-wave total-energy methodology with the generalized gradient approximation (GGA) [70]

for exchange–correlation, as implemented in the Vienna Ab initio Simulation Package [71–75]. The projector augmented wave with Perdew–Burke–Ernzerhof potentials was used with the spin-polarized method [76,77]. Unless otherwise specified, all structures were fully relaxed with respect to volume as well as all the internal atomic coordinates of the cell. The convergence of results with respect to energy cutoff and k-points was carefully considered. A plane-wave basis set was used with an energy cutoff of 300 eV to represent the Kohn–Sham wave functions. The summation over the Brillouin zone for the bulk structures was performed on a 0.13 (1/Å) spacing Monkhorst–pack k-point mesh for all calculations.

3. Results and discussion

3.1. Precipitate strengthening and nanostructure during isothermal aging at 275 and 300 °C

The precipitation behavior of both alloys during isothermal aging at 275 and 300 °C for aging times from 0.5 to 24 h is displayed in Fig. 1, as monitored by Vickers microhardness. The as-cast microhardness value of the high-Si alloy of 256 ± 5 MPa is greater than that of the low-Si alloy, 233 ± 12 MPa. The larger microhardness in the high-Si alloy is due in small part to the increased solid-solution strengthening provided by the additional 0.04 at.% Si. The difference in microhardness may also be a result of increased solute clustering due to the addition of Si, as discussed in Section 3.2. From Fig. 1, the microhardness values of the high-Si alloy are significantly larger than those of the low-Si alloy for the first 2 h of aging at 275 and 300 °C. For example, the microhardness values of samples aged for 1 h at 300 °C are 377 ± 12 and 320 ± 11 MPa for the high- and low-Si alloys, respectively. The measured strength increment due to precipitation at this aging time, estimated as $\Delta HV/3$ [78] (where ΔHV is the increase in microhardness

from the as-cast state to the aged state), is 40 ± 4 MPa for the high-Si alloy and 29 ± 6 MPa for the low-Si alloy, corresponding to an 11 MPa increase provided by the addition of 0.04 at.% Si. In contrast, the two alloys have the same microhardness values, within experimental error, for aging times >4 h at either 275 or 300 °C. The 0.04 at.% Si addition is not anticipated to increase alloy peak strength, since Si, which partitions preferentially to Al_3Sc ($L1_2$), and substitutes on the Al sublattice of the phase [35,79], does not increase the volume fraction of precipitates. The addition of Si accelerates precipitation in these dilute Al–Sc-based alloys, as observed by Beeri et al. for Al–Sc alloys with ~ 0.025 at.% Si, and Sc concentrations < 0.06 at.% Sc [18].

LEAP tomography of low- and high-Si samples aged for 1 h at 300 °C was performed to investigate the increase in precipitation kinetics due to increased Si concentrations; the reconstructions are displayed in Fig. 2. The high-Si alloy has a significantly larger number density N_v and volume fraction of precipitates ϕ of $4.8 \pm 0.6 \times 10^{22}$ m^{-3} and $0.026 \pm 0.004\%$, respectively, than the low-Si alloy, which has N_v and ϕ values of $0.87 \pm 0.31 \times 10^{22}$ m^{-3} and $0.008 \pm 0.005\%$, respectively (Table 2). The mean radii of the precipitates are comparable at 1.1 ± 0.3 and 1.3 ± 0.3 nm for the high- and low-Si alloys, respectively. The volume fractions measured after 1 h are smaller than the equilibrium values, owing to the short aging time. APT compositional measurements (Fig. 3) reveal that the precipitates have compositions close to $(Al,Si)_3Sc$, with a near-zero Zr content (Table 3). The precipitates in the high-Si alloy contain more Si than those in the low-Si alloy $(8.10 \pm 0.29$ vs 2.72 ± 0.42 at.% $^{28}Si^{2+})$. The larger Si content in the precipitates of the high-Si alloy is consistent with the observed acceleration in the precipitation of Sc, resulting in the higher microhardness values in this alloy at early aging times (Fig. 1).

To correlate the measured precipitate properties and microhardness values, the strength increments for order strengthening ($\Delta\sigma_{ord}$), coherency and modulus strengthening ($\Delta\sigma_{coh} + \Delta\sigma_{mod}$), or strengthening by the Orowan bypass mechanism ($\Delta\sigma_{Or}$), are calculated using the equations in Appendix A, and listed in Table 4. The predicted strengthening increments are compared with the measured strength increment, estimated as $\Delta HV/3$. The strengthening increment from precipitate shearing is taken as the larger of (a) the sum of modulus strengthening and coherency strengthening or (b) order strengthening. This is because the mechanisms in (a) and (b) occur sequentially as dislocations move towards the matrix/precipitate interface and shear the precipitates. Shearing and Orowan bypass occur in parallel, thus strengthening is dictated by the mechanism that requires the smallest stress. From Table 4, both order and coherency and modulus mismatch strengthening are predicted to be operative in both alloys after 1 h at 300 °C. The critical radius at which the deformation mechanism changes from precipitate shearing to an Orowan bypass mechanism is 1.5–2.0 nm in an Al–0.18 at.% Sc alloy [2,80]. Accordingly, for the high- and low-Si alloys,
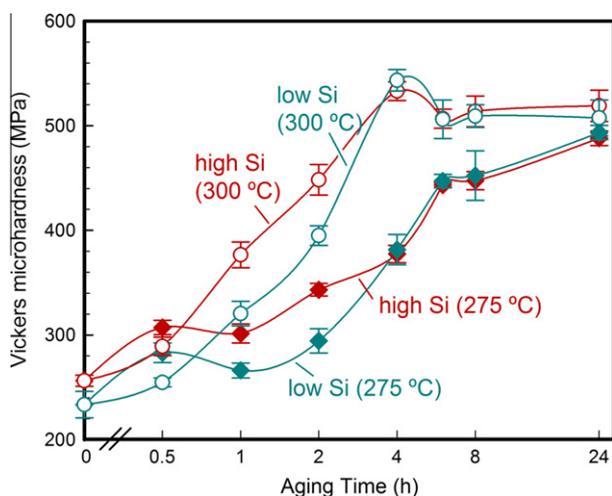
Fig. 1. Evolution of the Vickers microhardness during isothermal aging at 275 (dashed line) and 300 °C (solid line) for Al–0.06Zr–0.06Sc–0.06Si (high-Si alloy) and Al–0.06Zr–0.06Sc–0.02Si (low-Si alloy).
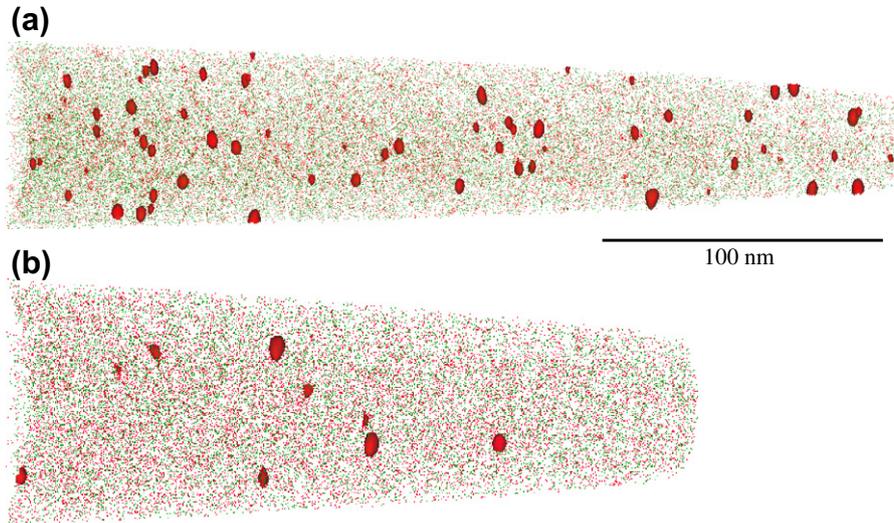
Fig. 2. Three-dimensional APT reconstructions of samples aged isothermally for 1 h at 300 °C for: (a) Al–0.06Zr–0.06Sc–0.06Si (high-Si alloy) and (b) Al–0.06Zr–0.06Sc–0.02Si (low-Si alloy). The precipitates are delineated with 2 at.% Sc (red) isoconcentration surfaces for visualization purposes. Scandium atoms are shown in red, Zr atoms in green and Al and $^{28}Si^{2+}$ atoms are omitted for clarity. (For interpretation of the references to color in this figure legend, the reader is referred to the web version of this article.)

Table 2
Precipitate number density N_v, mean radius $\langle R \rangle$, volume fraction ϕ, number of precipitates analyzed and Vickers microhardness HV for alloys with two heat treatments.

Alloy	Heat treatment	N_v ($\times 10^{22}$ m^{-3})	$\langle R \rangle$ (nm)	ϕ (%)	No. of precipitates[a]	HV (MPa)
Al–0.06Zr–0.06Sc–0.06Si	1 h/300 °C	4.8 ± 0.6	1.1 ± 0.3	0.026 ± 0.004	69	376 ± 12
Al–0.06Zr–0.06Sc–0.02Si	1 h/300 °C	0.87 ± 0.31	1.3 ± 0.3	0.008 ± 0.005	8	320 ± 12
Al–0.06Zr–0.06Sc–0.06Si	8 h/300 °C + 32 days/400 °C	1.3 ± 0.4	3.1 ± 0.5	0.322 ± 0.010	12.5	614 ± 22
Al–0.06Zr–0.06Sc–0.02Si	8 h/300 °C + 32 days/400 °C	2.3 ± 0.3	2.7 ± 0.5	0.337 ± 0.004	57	627 ± 9

[a] The number of precipitates analyzed is smaller than the total number of precipitates detected by APT. Precipitates that intersect the sample volume contribute 0.5 to the number density and are not included in the measurement of radius.

with mean precipitate radii of 1.1 ± 0.3 and 1.3 ± 0.3 nm, respectively, the shearing mechanism is predicted to be operative. Good agreement between experimental and predicted strengthening increments was also reported for Al–0.06 at.% Sc alloys with and without additions of Zr, Ti, Gd, Tb, Dy, Ho, Er, Tm, Yb, Lu and Li [2,64–66,81–84].

3.2. Solute–solute clustering during isothermal aging at 300 °C

The partial RDF analyses were used to study the effect of Si on precipitation kinetics. The partial RDF around Sc and Si atoms measured in the matrix of both alloys, for the samples aged isothermally at 300 °C for 1 h, are displayed in Fig. 4. In the high-Si alloy, Fig. 4 demonstrates that strong Si–Sc and Si–Si clustering exists at the first nearest-neighbor (NN) distance, along with Sc–Sc and Sc–Zr clustering over the first few NN distances, particularly at the second NN distance. Sc–Sc and Sc–Zr clustering at the second NN is expected for L1$_2$-type ordering, which may lead to precipitate nucleation. In the low-Si alloy, the partial RDF value for Si–Sc is greater than unity over the first few NN distances, indicating their clustering, though not as extensively as in the high-Si alloy. Clustering

of Sc–Sc and Sc–Zr occurs over the first few NN distances, though to a lesser extent than in the high-Si alloy. Strong Si–Si clustering for the first few NN distances is also observed in the low-Si alloy.

The solute–solute binding energies are calculated from first-principles to determine the energetic driving force for the solute clustering measured experimentally. The binding energy between solutes X and Y in Al separated by the ith NN distance, $E_{i,Al}^{X-Y\ bind}$ is calculated employing:

$$E_{i,Al}^{X-Y\ bind} = E_{i,Al}^{X+Y} - (E_{Al}^X + E_{Al}^Y) \qquad (2)$$

where $E_{i,Al}^{X+Y}$ is the total energy of the Al-supercell of 64 atoms, where the X and Y atoms are separated by the ith NN distance, and E_{Al}^X and E_{Al}^Y are the total energy of the 32-atom Al supercell, with solutes X and Y replacing one Al atom, respectively. The calculated solute–solute binding energies are listed in Table 5. The sign convention whereby positive binding energies indicate energetically favorable binding is adopted. These values predict an attractive (positive) binding energy for Si–Si (0.14 eV pair^{-1}), Si–Sc (0.33 eV pair^{-1}) and Si–Zr (0.18 eV pair^{-1}) at the first NN site, and for Sc–Sc (0.18 eV pair^{-1}), Zr–Zr (0.24 eV pair^{-1}) and Sc–Zr (0.12 eV pair^{-1}) at the second NN site. The Si–Sc binding energy, which is attractive
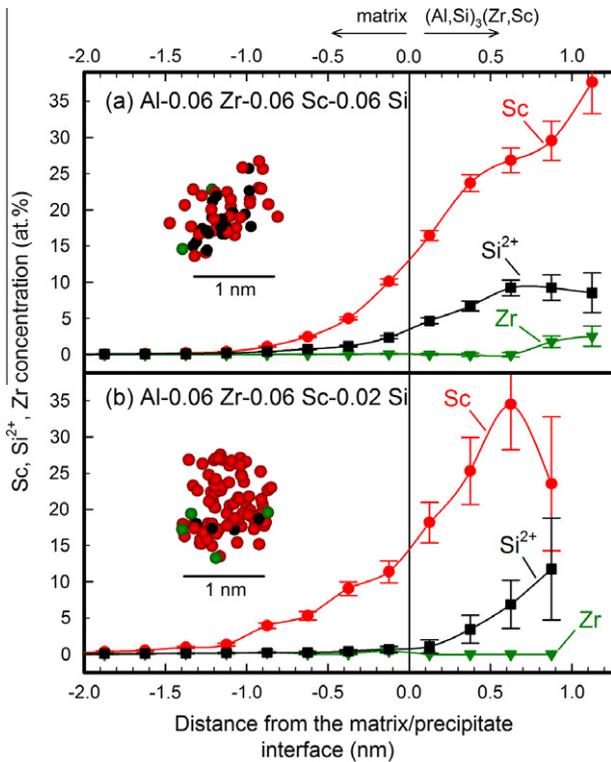
Fig. 3. Concentration profiles across the α-Al matrix/precipitate interface for samples aged isothermally for 1 h at 300 °C for: (a) Al–0.06Zr–0.06Sc–0.06Si (high-Si alloy) and (b) Al–0.06Zr–0.06Sc–0.02Si (low-Si alloy). The inset images in (a) and (b) are APT reconstructions of a representative precipitate from each alloy. Scandium atoms are shown in red, Zr atoms are in green, Si^{2+} atoms are in black, and the Al atoms are omitted for clarity. (For interpretation of the references to color in this figure legend, the reader is referred to the web version of this article.)

at the first NN distance, is also attractive (0.13 eV defect pair^{-1}) at the second NN site. The calculated binding energies accurately predict the Si–Si and Si–Sc binding at the first NN site, as well as Sc–Sc and Sc–Zr binding at the second NN site, observed experimentally in

the partial RDF results (Fig. 4). The solute–solute clustering observed in the partial RDF is a result of these binding energies, but the extent of clustering is limited by the diffusivities of the solute species involved, because they must have sufficient time to reach one another at the aging temperature.

3.3. Solute–vacancy binding energies

Experimental evidence for Si–Sc clustering employing the partial RDF methodology has been presented, and the energetic driving force for this clustering has been determined through calculations of the Si–Sc binding energy. Solute–vacancy binding is now considered, which can result in changes in the vacancy distribution in Al, resulting in differences between the vacancy concentration close to a solute atom and in the Al bulk. The solute–vacancy binding energy $E_{i,Al}^{X-v\ bind}$ is given by

$$E_{i,Al}^{X-v\ bind} = E_{i,Al}^{v+X} - (E_{Al}^{X} + E_{Al}^{v}) \tag{3}$$

where $E_{i,Al}^{v+X}$ is the total energy of the supercell with 64 atoms, where the solute atom of species X and the vacancy v are separated by the ith NN distance, and E_{Al}^{X} and E_{Al}^{v} are the total energies of the 32-atom Al supercell with the X atom and vacancy replacing one Al atom, respectively. The calculated values of the solute–vacancy binding energies are presented in Table 6, and compared with those calculated by Wolverton employing a 64-atom cell and the local-density approximation (LDA) (Sc and Zr) and GGA (Si) methods [36] and by Simonovic and Sluiter with a 64-atom cell and the GGA method [37]. The present Si–vacancy binding energy of 0.12 eV vacancy^{-1} is attractive, while the values for Sc–vacancy of –0.25 and for Zr–vacancy of –0.31 eV vacancy^{-1} are repulsive. The same trends (sign of the energy) were predicted previously by Wolverton [36] and Simonovic and Sluiter [37], confirming that it is favorable for a vacancy to bind to a Si atom, while it is unfavorable for a vacancy to be next to a Sc or Zr atom.

Table 3
Precipitate and matrix compositions for alloys with two heat treatments, as determined by APT.

Alloy	Heat treatment	Precipitate composition (at.%)				Matrix composition (at.ppm)		
		Al	Zr	Sc	$^{28}Si^{2+}$	Zr	Sc	$^{28}Si^{2+}$
Al–0.06Zr–0.06Sc–0.06Si	1 h/300 °C	62.56 ± 0.51	0.09 ± 0.03	29.25 ± 0.48	8.10 ± 0.29	486 ± 12	431 ± 7	363 ± 7
Al–0.06Zr–0.06Sc–0.02Si	1 h/300 °C	63.81 ± 1.25	0.14 ± 0.10	33.33 ± 1.23	2.72 ± 0.42	563 ± 6	535 ± 6	72 ± 2
Al–0.06Zr–0.06Sc–0.06Si	8 h/300 °C + 32 days/400 °C	69.93 ± 0.31	8.23 ± 0.19	20.88 ± 0.28	0.97 ± 0.07	75 ± 17	30 ± 4	284 ± 10
Al–0.06Zr–0.06Sc–0.02Si	8 h/300 °C + 32 days/400 °C	69.20 ± 0.14	5.19 ± 0.07	25.37 ± 0.13	0.25 ± 0.01	22 ± 7	65 ± 3	107 ± 4

Table 4
Experimental and calculated strength increments for alloys with two heat treatments.

Alloy	Heat treatment	$\Delta HV/3$ (MPa)	$(\Delta\sigma_{ord})$ (MPa)	$(\Delta\sigma_{coh} + \Delta\sigma_{mod})$ (MPa)	$(\Delta\sigma_{Or})$ (MPa)
Al–0.06Zr–0.06Sc–0.06Si	1 h/300 °C	40 ± 4	38 ± 3	38 ± 3	62 ± 25
Al–0.06Zr–0.06Sc–0.02Si	1 h/300 °C	29 ± 6	21 ± 7	22 ± 2	32 ± 14
Al–0.06Zr–0.06Sc–0.06Si	8 h/300 °C + 32 days/400 °C	119 ± 8	133 ± 2	162 ± 7	128 ± 29
Al–0.06Zr–0.06Sc–0.02Si	8 h/300 °C + 32 days/400 °C	131 ± 5	137 ± 1	159 ± 7	143 ± 37
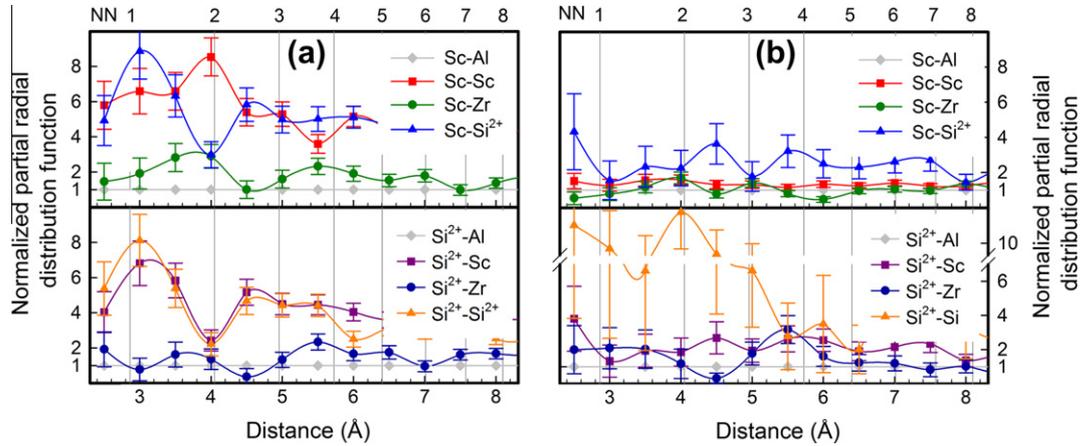
Fig. 4. Partial RDF with respect to Sc (top) and Si (bottom) in the matrix of: (a) Al–0.06Zr–0.06Sc–0.06Si (high-Si alloy); (b) Al–0.06Zr–0.06Sc–0.02Si (low-Si) aged isothermally at 300 °C for 1 h. In the high-Si alloy, strong Si–Sc and Si–Si clustering is detected at the first NN distance, along with strong Sc–Sc and some Sc–Zr clustering at the second NN distance. In the low-Si alloy, there is no evidence of Sc–Si clustering at the first NN distance, though Si–Si clustering at this distance is strong.

Table 5
Solute–solute (X–Y) binding energies in Al, $E_{i,Al}^{X-Ybind}$, from first-principles calculations at the first and second NN distances; the sign convention is adopted that positive binding energies are attractive, indicating energetically favorable binding.

Solute–solute pair	$E_{i,Al}^{X-Ybind}$ (eV atom^{-1})	
	NN	2NN
Si–Si	0.14	−0.11
Sc–Sc	−0.39	0.18
Zr–Zr	−0.36	0.24
Sc–Zr	−0.47	0.12
Si–Sc	0.33	0.13
Si–Zr	0.18	−0.12

Table 6
Solute–vacancy binding energies in Al, $E_{i,Al}^{X-vbind}$ from first-principles calculations at the first NN distance, employing a 64-atom cell for Sc and Zr (LDA) and Si (GGA); the sign convention is adopted that positive binding energies are attractive and therefore energetically favorable.

Solute–solute pair	$E_{i,Al}^{X-vbind}$ (eV vacancy^{-1})	
	Present study	Previous calculations
Si–v	0.12	0.08[a], 0.05[b]
Sc–v	−0.25	−0.17[a], −0.12[b]
Zr–v	−0.31	−0.28[a], −0.20[b]

[a] The values are compared with those previously calculated by Wolverton (LDA for Zr an Sc, and GGA for Si) [36].
[b] The values are compared with those previously calculated by Simonovic and Sluiter (GGA for Zr, Sc and Si) [37].

Because the precipitates that have evolved after 1 h of aging at 300 °C in both the low- and high-Si alloys are enriched in Sc and Si, analysis of the nucleation behavior focuses on these two solute species. This paper has presented experimental and simulated evidence for Si–Sc clustering in Al, and demonstrated through solute–vacancy binding energy calculations that a vacancy is more likely to be in the proximity of a Si atom. These findings suggest that the addition of Si to dilute Al–Sc systems will increase the local vacancy concentration close to a Sc–Si dimer.

Given the experimental and simulated evidence for Si–Sc binding, the binding energy of a vacancy v to a Sc–Si pair was also calculated. Twelve possible arrangements of Si, Sc and v were constructed in a 64-atom supercell, within which Si, Sc and v were connected to at least one of the other species of interest, in both linear and non-linear chains. The most favorable configuration, consisting of Sc and v separated by Si, all in a linear chain (Sc–Si–v), yields a binding energy of −0.08 eV vacancy^{-1}. The least favorable configuration, where the Sc, Si and v are all NN with one another, gives a binding energy of −0.17 eV vacancy^{-1}. These values are both more positive than the Sc–v binding energy in the absence of Si of −0.25 eV atom^{-1}, and thus a vacancy is more likely to be in the vicinity of a Sc atom when it is bound to Si. It is noted that, while the calculated Sc–v binding energy increases due to the addition of Si, binding of Sc and v remains repulsive.

There is little experimental evidence for Si–Zr clustering in the matrix over the first few NN distances from the partial RDF analyses (Fig. 4). Additionally, the Zr concentration in precipitates after 1 h of aging at 300 °C is the same in both alloys, within experimental error, (0.09 ± 0.03 at.% for the high-Si alloy and 0.14 ± 0.10 at.% for the low-Si alloy). Thus, unlike Sc, the precipitation of Zr does not appear to be accelerated by the addition of Si. The calculated Si–Zr binding energies of 0.18 (1st NN) and −0.12 eV pair^{-1} (2nd NN) make Si–Zr binding less favorable than Si–Sc, which has more attractive (positive) binding energies of 0.33 (1st NN) and 0.13 eV pair^{-1} (2nd NN). It is noted that the presence of Sc in the present alloys may have scavenged Si, and thus limited both Si–Zr binding and the acceleration of the precipitation of Zr. Accelerating the precipitation kinetics of Zr would make less expensive, Sc-free, Al–Zr-based alloys more viable. Future investigation of other elements, such as Sn, In, Ge or Cd, which have been shown to accelerate precipitation kinetics in other Al alloys [36,85], is therefore warranted.

3.4. Effect of Si on the vacancy formation energy and Sc migration energy

To understand completely the effect of Si on the precipitation kinetics of Sc, this study examines its role in altering the activation barrier for diffusion of Sc. The diffusivity of vacancy-mediated diffusion of an impurity in Al at temperature T (K) is given by

$$D = D_0 f_e \left(\frac{-E_f^{v-X} - E_m^v}{k_B T} \right) \qquad (4)$$

where D_0 is a prefactor, f is the dimensionless correlation factor, k_B is Boltzmann's constant, E_f^{v-X} is the vacancy formation energy next to an impurity atom X, and E_m^v is the impurity migration energy mediated by a vacancy. The vacancy formation energy for a given impurity is the difference between the vacancy formation energy in Al and the relevant solute–vacancy binding energy (Table 6). The vacancy formation energy in Al, E_f^v, is calculated from

$$E_f^v = E_{(v+(n-1)Al)}^{tot} - \frac{(n-1)}{n} E_{nAl}^{tot} \qquad (5)$$

where $E_{(v+(n-1)Al)}^{tot}$ is the total energy of the supercell with $n = 32$ Al atoms with one vacancy substituted for one Al atom, and E_{nAl}^{tot} is the total energy of the supercell with n Al atoms. The calculated vacancy formation energy is 0.65 eV vacancy^{-1}, which is comparable with the experimentally measured value of 0.66 eV vacancy^{-1} [86–88] and with other calculated values of 0.5–0.7 eV vacancy^{-1} [37,50,89–93]. Vacancy formation energies near Si, E_f^{v-Si}, of 0.53 eV vacancy^{-1}, and near Sc, E_f^{v-Sc}, of 0.90 eV vacancy^{-1}, are calculated by subtracting the relevant solute–vacancy binding energy. Therefore, as discussed in Section 3.3, a vacancy is more likely to be found near a Si atom than near a Sc atom.

Early-stage precipitation in these alloys is limited by the vacancy-mediated diffusion of Sc, which is controlled by the migration energy from the initial atomic position of Sc, through the saddle-point configuration, to its final position. The migration energy of Sc in Al, E_m^{Sc}, is calculated from first principles by subtracting the initial energy E_{IS}^{tot} from the energy of the unstable saddle point E_{SP}^{tot}, employing a transition state structure search using the climbing image nudged elastic band method [94]:

$$E_m^{Sc} = E_{SP}^{tot} - E_{IS}^{tot} \qquad (6)$$

The values of E_m^{Sc} for a Sc-vacancy exchange in (i) pure Al and (ii) in Al, where Si–Sc binding occurs at the 1st NN position after a solute–vacancy exchange, are indicated in Fig. 5. The value of E_m^{Sc} is decreased from 0.74 to 0.45 eV atom^{-1} by the formation of a Sc–Si pair after solute–vacancy exchange. Additionally, an overall energy decrease of 0.05 eV atom^{-1} is predicted for the atomic configuration that results from a Sc–vacancy exchange resulting in Si–Sc binding. Thus, the addition of Si decreases the energy of the transition state, thereby significantly
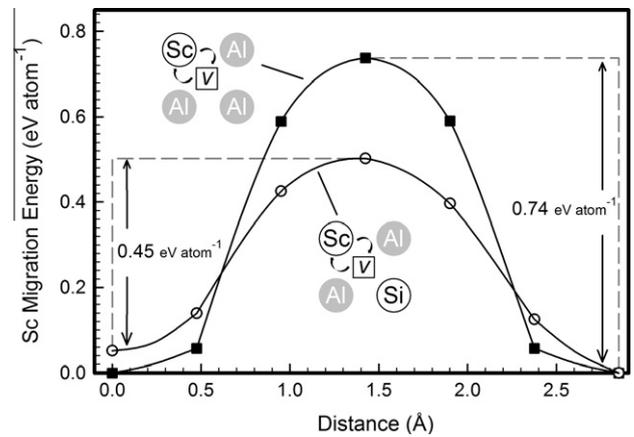
Fig. 5. Migration energy of Sc in (i) pure Al and (ii) in Al, where Sc–Si binding occurs at the first NN distance after vacancy–solute exchange, as calculated by the DFT-GGA method at 0 K. The migration energy decreases from 0.74 to 0.45 eV atom^{-1} owing to strong Si–Sc binding.

reducing the migration energy of Sc. The value of E_m^{Sc} of 0.74 eV atom^{-1} in the absence of Si is comparable with the values of E_m^{Sc} of ~0.6 and ~0.7 eV atom^{-1} calculated by Sandberg and Holmstad, employing LDA and GGA, respectively [50], and 0.66 eV atom^{-1} by Simonovic and Sluiter using GGA [37].

3.5. Precipitate structure after two-stage isothermal aging at 300 and 400 °C

To determine the effects of Si on the precipitate nanostructure and composition after longer aging times, LEAP tomography of low- and high-Si samples aged isothermally for 8 h at 300 °C and 32 days at 400 °C was performed (Figs. 6 and 7). Both alloys have a precipitate structure consisting of a Sc-enriched core and Zr-enriched shell, as observed in prior studies of Al–Sc–Zr alloys [11–17,95–98]. The spheroidal precipitates in the high-Si alloy have an average radius $\langle R \rangle$ of 3.1 ± 0.5 nm, a number density N_v of $1.3 \pm 0.4 \times 10^{22}$ m^{-3} and a volume fraction ϕ of $0.322 \pm 0.010\%$ (Table 2). The spheroidal precipitates in the low-Si alloy have an average radius of 2.7 ± 0.5 nm, a number density of $2.3 \pm 0.3 \times 10^{22}$ m^{-3} and a volume fraction of $0.337 \pm 0.004\%$. The measured microhardness values after two-stage aging are 614 ± 22 and 627 ± 9 MPa for the high- and low-Si alloys, respectively, and Orowan strengthening is therefore operative in both alloys (Table 4) employing the methodology described in Section 3.1.

The number density of precipitates in the high-Si alloy decreased from $4.8 \pm 0.6 \times 10^{22}$ m^{-3} after 1 h of aging at 300 °C to $1.3 \pm 0.4 \times 10^{22}$ m^{-3} after 8 h at 300 °C and 32 days at 400 °C, implying precipitate coarsening. The number density in the low-Si alloy increased from 0.87 ± 0.31 to $2.3 \pm 0.3 \times 10^{22}$ m^{-3} after the same aging treatment, indicating that precipitate nucleation continued in the low-Si alloy after 1 h of aging, before precipitate growth and coarsening commenced. The larger Si supersaturation in the high-Si alloy increases the nucleation current
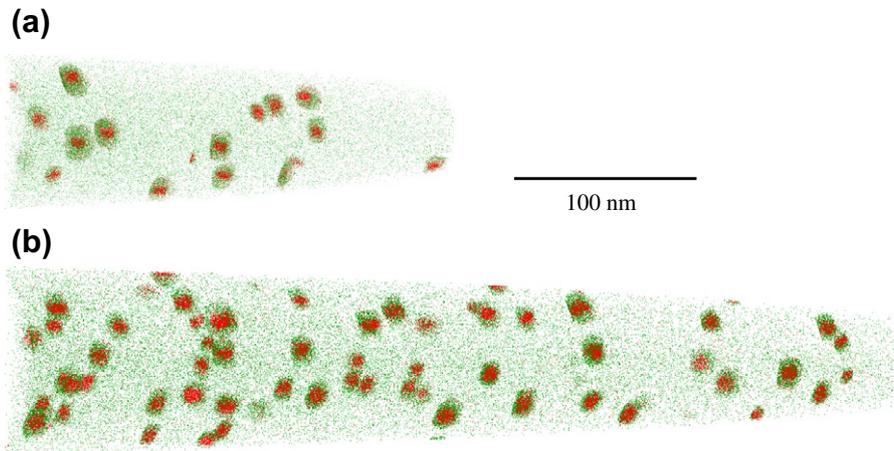
Fig. 6. Three-dimensional APT reconstructions of samples subjected to a two-stage aging treatment of 300 °C for 8 h and then 400 °C for 32 days for: (a) Al–0.06Zr–0.06Sc–0.06Si (high-Si alloy); (b) Al–0.06Zr–0.06Sc–0.02Si (low-Si alloy). Scandium atoms are shown in red, Zr atoms are green, and Al and Si^{2+} atoms are omitted for clarity. (For interpretation of the references to color in this figure legend, the reader is referred to the web version of this article.)
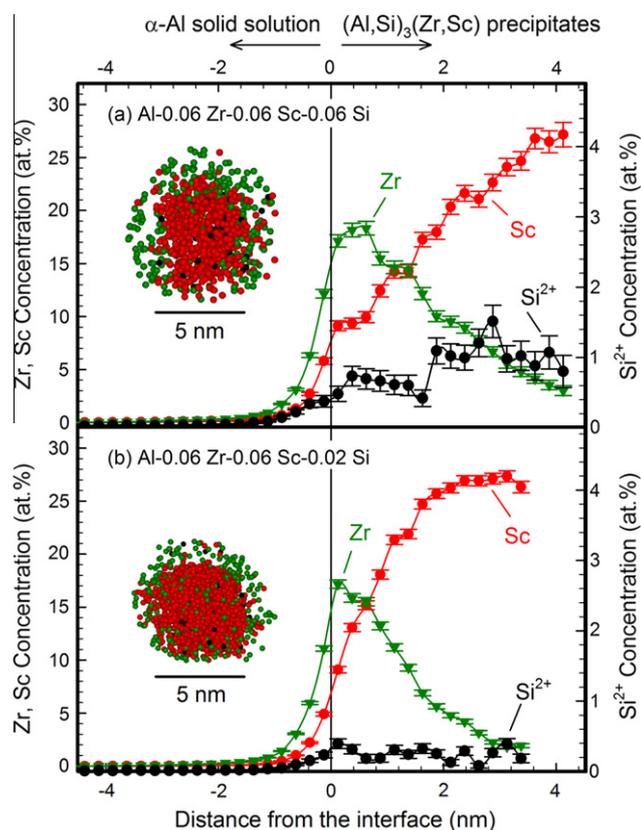
Fig. 7. Concentration profiles across the α-Al matrix/precipitate interface for samples subjected to a two-stage aging treatment of 300 °C for 8 h and 400 °C for 32 days for: (a) Al–0.06Zr–0.06Sc–0.06Si (high-Si alloy); (b) Al–0.06Zr–0.06Sc–0.02Si (low-Si alloy). The inset images in (a) and (b) are APT reconstructions of a representative precipitate from each alloy. Scandium atoms are shown in red, Zr atoms in green, Si^{2+} atoms are in black, and the Al atoms are omitted for clarity. (For interpretation of the references to color in this figure legend, the reader is referred to the web version of this article.)

at 300 °C. Thus, the precipitates coarsen for longer at 300 °C, before they are rendered coarsening resistant by the precipitation of the Zr-enriched shell at 400 °C. As a result, the high-Si alloy has a smaller number density of $1.3 \pm 0.4 \times 10^{22}$ m^{-3} compared with the value for the low-Si alloy of $2.3 \pm 0.3 \times 10^{22}$ m^{-3} after two-stage iso-thermal aging, despite the fact that the alloys have compa-rable precipitate volume fractions of $0.322 \pm 0.010\%$ and $0.337 \pm 0.004\%$, respectively. A more complete study of the temporal evolution of the alloys would provide a more quantitative description of the acceleration of the kinetic pathways that lead to precipitation in these alloys, which warrants future research.

The precipitate and matrix compositions of the alloys after two-stage aging (Table 3) demonstrate that Si, Zr and Sc partition to the precipitate phase. Given the difficul-ties in measuring accurately the concentration of Si with LEAP tomography (Section 2.2), this study is limited to qualitative analyses of Si partitioning. The high-Si alloy has a larger Si concentration in both the matrix and precip-itate phases, as anticipated. It is noted that the Si concen-tration in the Sc-enriched core is larger by a factor of ~2 than in the Zr-enriched shell in the high-Si alloy (Fig. 7), a result that is not observed in the low-Si alloy.

3.6. Silicon phase partitioning and site substitution

To gain insight into the energetic driving force for the partitioning of Si to the precipitates and for the preference of Si for the Sc-enriched core (Fig. 8), the Si-site substitu-tion energies are computed across the Al(fcc)/Al$_3$Sc(L1$_2$) and Al(fcc)/Al$_3$Zr(L1$_2$) interfaces. These energies are com-puted using Al, Al$_3$Z and Al/Al$_3$Z fully relaxed supercells, where Z is either Sc or Zr. The ordered-phase substitu-tional structures were modeled by allowing Si to substitute on either the Al or Z (solute) sublattice in the Al$_3$Z (L1$_2$) superlattice, and permitting the structures to relax fully. The Si substitutional energies $E_{\text{Si}\rightarrow\text{Al}}^{\text{Al}_3\text{Z}}$ and $E_{\text{Si}\rightarrow\text{Al}}^{\text{Al}_3\text{Z}}$, in Al$_3$Z are defined as follows:

$$E_{\text{Si}\rightarrow\text{Al}}^{\text{Al}_3\text{Z}} = \left[\left(E_{(\text{Al}_{1-x}\text{Si}_x)_3\text{Z}}^{tot} + n_{\text{Al}}\mu_{\text{Al}} \right) - \left(E_{\text{Al}_3\text{Z}}^{tot} + n_{\text{Si}}\mu_{\text{Si}} \right) \right] \quad (7)$$
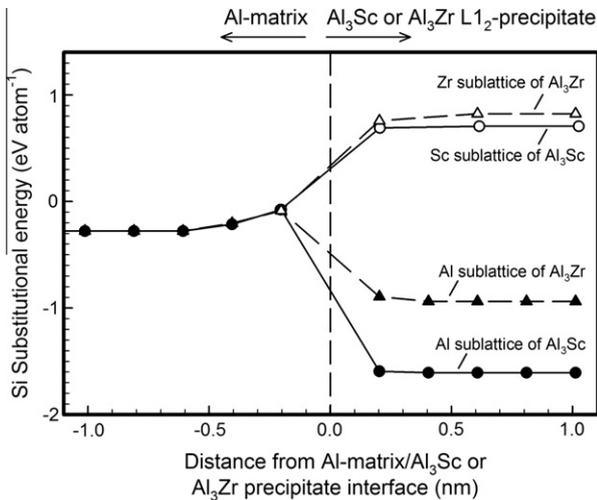
Fig. 8. Substitutional energy of Si as a function of distance from the Al matrix/Al$_3$Sc (L1$_2$) or Al matrix/Al$_3$Zr (L1$_2$) precipitate interfaces, where Si can occupy either the Al or Sc sublattice site of either the Al$_3$Sc or Al$_3$Zr precipitate phases, as calculated by the DFT-GGA method at 0 K. Silicon from the Al matrix is predicted to partition preferentially to the Al sublattice sites of Al$_3$Sc.

$$E_{Si\rightarrow Z}^{Al_3Z} = \left[\left(E_{Al_3(Z_{1-y}Si_y)}^{tot} + n_Z\mu_Z \right) - \left(E_{Al_3Z}^{tot} + n_{Si}\mu_{Si} \right) \right] \quad (8)$$

where E^{tot} is total energy before and after substitution, x and y are the fraction substituted for (herein, only one substitutional atom is used, so $x = 1/24$ and $y = 1/8$), and μ is the chemical potential. The chemical potential from the dilute solution Al$_{31}$Z and Al in equilibrium state is calculated: $\mu_Z = E_{Al_3Z} - 31E_{Al}$.

The energies associated with the substitution of Si onto the Al sublattice sites of either of the precipitate phases (Al$_3$Sc or Al$_3$Zr) are significantly smaller than at the solute sublattice sites. Additionally, there is a significant energetic driving force for the partitioning of Si from the matrix to the Al sublattice sites of the precipitates: 1.33 and 0.66 eV atom^{-1} for Al$_3$Sc and Al$_3$Zr, respectively. Thus, Si is predicted to partition preferentially to the precipitates, as observed experimentally (Table 3), and to occupy the Al sublattice sites of the ordered phases, as determined previously by first-principles calculations for Al$_3$Sc [35,79]. Thus, the addition of Si increases the thermodynamic driving force for the precipitation of Al$_3$Sc, which should further accelerate the precipitation kinetics in these alloys. Additionally, the difference of 0.67 eV atom^{-1} between the energetic driving forces for Si partitioning to Al$_3$Sc and Al$_3$Zr results in the higher Si concentrations measured in the Sc-rich Al$_3$(Sc,Zr) core compared with the Zr-rich Al$_3$(Zr,Sc) shell (Fig. 7). Previous first-principles calculations by Du et al. [35] found a significantly smaller driving force of 0.15 eV atom^{-1} for the partitioning of Si to the Al sublattice site of the Al$_3$Sc (L1$_2$) phases. In their calculations, the reference states for Si and Sc are those of pure elements, which leads to a much smaller calculated driving force compared with the present value of 1.33 eV atom^{-1}.

4. Conclusions

The effect on the precipitate evolution of Al–0.06 Sc–0.06 Zr at.% of adding 0.02 or 0.06 at.% Si was studied by microhardness and APT to determine the effect of Si on accelerating precipitation in dilute Al–Sc alloys. These results are complemented with first-principles calculations of the solute–solute and solute–vacancy binding energies, and the migration energy of Sc to elucidate the role of Si in accelerating precipitation kinetics. This research leads to the following conclusions.

1. The additional 0.04 at.% Si in the high-Si alloy results in a more rapid increase in microhardness at 275 and 300 °C at early aging times (<4 h), compared with the low-Si alloy. This difference is explained by LEAP tomography of samples aged for 1 h at 300 °C, which reveals that the high-Si alloy has a significantly larger number density and volume fraction of precipitates than the low-Si alloy.
2. Partial RDF analyses of the matrix of the high-Si alloy aged for 1 h at 300 °C reveals considerable Si–Sc and Si–Si clustering at the first NN distance, and Sc–Sc and Sc–Zr clustering at the second NN distance. There is significantly less Si–Sc, Sc–Sc or Sc–Zr clustering in the low-Si alloy.
3. First-principles calculations of solute–solute binding energies agree with the results of the partial RDF analyses: Si–Si and Si–Sc binding at the first NN distance is calculated to be attractive (positive values), with binding energies of 0.14 and 0.33 eV pair^{-1}, respectively. The second NN Si–Sc binding energy of 0.13 eV pair^{-1} implies that Si–Sc binding is also attractive at the second NN distance. Binding of Sc–Sc and Sc–Zr at the second NN distance is calculated to be attractive, and is indicative of L1$_2$-type ordering, with binding energies of 0.18 and 0.12 eV pair^{-1}, respectively.
4. First-principles calculations reveal that a vacancy is more likely to be in the vicinity of a Sc atom when it is bound to Si. The most favorable configuration, consisting of Sc and v separated by Si, all in a linear chain (Sc–Si–v), yields a binding energy of -0.08 eV vacancy^{-1}. The least favorable configuration, where the Sc, Si and v are all NN with one another, gives a binding energy of -0.17 eV vacancy^{-1}. These values are both more positive than the Sc–v binding energy in the absence of Si of -0.25 eV atom^{-1}.
5. The addition of Si to Al–Sc alloys alters the energy of the transition state during Sc diffusional migration, significantly reducing the migration energy. The calculated value of the Sc migration energy is decreased from 0.74 eV atom^{-1} in the absence of Si, to 0.45 eV atom^{-1} for a configuration that results in Si–Sc binding following a Sc–vacancy exchange.
6. LEAP tomography of a high-Si alloy aged isothermally for 8 h at 300 °C and 32 days at 400 °C, which formed precipitates with a structure consisting of a Sc-enriched

core and a Zr-enriched outer shell, reveals Si partitioning to the precipitates. First-principles calculations predict accurately that Si partitions preferentially to the precipitates, and demonstrates that Si occupies the Al sublattice sites of the $L1_2$ ordered phases.

7. First-principles calculations indicate that the addition of Si accelerates the precipitation of Sc by binding with Sc atoms, decreasing both the vacancy formation energy near Sc, and the Sc migration energy in Al. Additionally, the calculated thermodynamic driving force for the partitioning of Si to the Al sublattice site of Al_3Sc ($L1_2$) further accelerates the precipitation kinetics of Sc in $(Al,Si)_3Sc$ ($L1_2$) precipitates.

Acknowledgements

Appendix A

The strength increments for order strengthening ($\Delta\sigma_{\text{ord}}$), coherency and modulus strengthening ($\Delta\sigma_{\text{coh}} + \Delta\sigma_{\text{mod}}$), and strengthening by the Orowan bypass mechanism ($\Delta\sigma_{\text{Or}}$) are calculated employing the methodology described in Refs. [2,99,100].

The contribution to the yield strength from order strengthening is given by

$$\Delta\sigma_{\text{ord}} = 0.81 M \frac{\gamma_{\text{APB}}}{2b} \left(\frac{3\pi\phi}{8} \right)^{1/2} \tag{A1}$$

where $M = 3.06$ is the mean matrix orientation factor for Al [101], $b = 0.286$ nm is the magnitude of the fcc matrix Burgers vector [102], ϕ is the volume fraction of precipitates, and $\gamma_{\text{ABP}} = 0.5$ J m^{-2} is an average value of the Al_3Sc anti-phase boundary (APB), energy for the $\{1\,1\,1\}$ plane [103–105].

The increase is yield strength due to coherency strengthening is given by

$$\Delta\sigma_{\text{coh}} = M \alpha_\varepsilon (G\varepsilon)^{3/2} \left(\frac{\langle R \rangle \phi}{0.5 \, Gb} \right)^{1/2} \tag{A2}$$

where $\alpha_\varepsilon = 2.6$ is a constant [99], $\langle R \rangle$ is the mean precipitate radius, $G = 25.4$ GPa [102] is the shear modulus of Al. For the samples aged for 1 h at 300 °C, the constrained lattice parameter mismatch ε is taken to be that of Al_3Sc ($L1_2$) in Al of 1.32% at room temperature [7]. For coherency strengthening in the samples aged 8 h at 300 °C and 32 days at 400 °C, the lattice parameter mismatch is that of Al_3Zr in Al of +0.75% at room temperature [7], to approximate the Zr-enriched shell that exists on the peripheral surface of the Al_3Sc precipitates. This provides a lower bound for the coherency strengthening increment, since it is expected that Sc contributes more significantly to coherency strengthening than does Zr. The calculation of an upper bound for coherency strengthening is unnecessary, since the Orowan bypass mechanism is the dominant precipitation strengthening mechanism, as it requires a smaller stress than the calculated lower bound for $\Delta\sigma_{\text{coh}}$ for the alloys that underwent two-stage isothermal aging (Table 4).

Strengthening by modulus mismatch is given by

$$\Delta\sigma_{\text{mod}} = 0.0055 M (\Delta G)^{3/2} \left(\frac{2\phi}{Gb^2} \right)^{1/2} b \left(\frac{\langle R \rangle}{b} \right)^{\left(\frac{3m}{2}-1\right)} \tag{A3}$$

where $\Delta G = 42.5$ GPa is the shear modulus mismatch between the matrix and the precipitates [106], and m is a constant, taken to be 0.85 [99].

Finally, the increase in yield strength for the Orowan bypass mechanism is given by

$$\Delta\sigma_{\text{Or}} = M \frac{0.4}{\pi} \frac{Gb}{\sqrt{1-v}} \frac{\ln\left(\frac{2r}{b}\right)}{\lambda} \tag{A4}$$

where $v = 0.34$ is Poisson's ratio for the matrix [101], and λ is the edge-to-edge interprecipitate distance, which is taken as the square lattice-spacing in parallel planes [107]:

$$\lambda = \left[\left(\frac{3\pi}{4\phi} \right)^{1/2} - 1.64 \right] \langle R \rangle \tag{A5}$$

Appendix B. Supplementary data

Supplementary data associated with this article can be found, in the online version, at http://dx.doi.org/10.1016/j.actamat.2012.05.036.

References

[1] Marquis EA, Seidman DN. Acta Mater 2001;49:1909.
[2] Seidman DN, Marquis EA, Dunand DC. Acta Mater 2002;50:4021.
[3] Royset J, Ryum N. Int Mater Rev 2005;50:19.
[4] Drits ME, Ber LB, Bykov YG, Toropova LS, Anastas'eva GK. Phys Met Phys Metall 1984;57:1172.
[5] Drits ME, Dutkiewicz J, Toropova LS, Salawa J. Cryst Res Technol 1984;19:1325.

[6] Sawtell RR, Morris J. Exploratory alloy development in the system Al–Sc–X. In: Kim Y-W, Griffith WM, editors. Dispersion strengthened aluminum alloys. Warrendale (PA): TMS; 1988. p. 409.
[7] Knipling KE, Dunand DC, Seidman DN. Z Metallkd 2006;97:246.
[8] Mao Z, Chen W, Seidman DN, Wolverton C. Acta Mater 2011;59:3012.
[9] Mao ZG, Seidman DN, Wolverton C. Acta Mater 2011;59:3659.
[10] Toropova LS, Eskin DG, Kharakterova ML, Dobatkina TV. Advanced aluminum alloys containing scandium: structure and properties. Amsterdam: OPA/Gordon & Breach Science Publishers; 1998.
[11] Elagin VI, Zakharov VV, Pavlenko SG, Rostova TD. Phys Met Phys Metall 1985;60:97.
[12] Tolley A, Radmilovic V, Dahmen U. Scr Mater 2005;52:621.
[13] Forbord B, Lefebvre W, Danoix F, Hallem H, Marthinsen K. Scr Mater 2004;51:333.
[14] Clouet E, Lae L, Epicier T, Lefebvre W, Nastar M, Deschamps A. Nat Mater 2006;5:482.
[15] Clouet E, Nastar M, Sigli C. Phys Rev B 2004;69:064109.
[16] Fuller CB, Murray JL, Seidman DN. Acta Mater 2005;53:5401.
[17] Toropova LS, Eskin D, Kharakterova M, Dobatkina T. Advanced aluminum alloys containing scandium: structure and properties. Gordon & Breach Science Publishers; 1998.
[18] Beeri O, Dunand DC, Seidman DN. Mater Sci Eng A 2010;A527:3501.
[19] Malek P, Janecek M, Smola B. Kovove Mater 2000;38:160.
[20] Hori S, Furushiro N, Fujitani W. J Jpn Inst Met 1981;31:649.
[21] Hallem H, Forbord B, Marthinsen K. Mater Sci Eng A 2004;A387–A389:940.
[22] Mitlin D, Radmilovic V, Morris Jr JW. Metall Mater Trans A 2000;31A:2697.
[23] Perry AJ, Entwistle KM. Philos Mag 1968;18:1085.
[24] Sato T, Kamio A, Lorimer GW. Mater Sci Forum 1996;217–222:895.
[25] Ohashi T, Ichikawa R. J Jpn Inst Met 1970;34:604.
[26] Hori S, Kondo T, Ikeno S. J Jpn Inst Met 1978;28:79.
[27] Tyvanchuk AT, Yanson TI, Kotur BA, Zarechnyuk OS, Kharakterova ML. Russ Metall 1988;4:190.
[28] Elagin VI, Zakharov VV, Rostova TD. Met Sci Heat Treat 1993;6:317.
[29] Elagin VI, Zakharov VV, Rostova TD. Met Sci Heat Treat 1992.
[30] Royset J, Hovland H, Ryum N. Mater Sci Forum 2002;396–402:619.
[31] Davydov VG, Rostova TD, Zakharov VV, Filatov YA, Yelagin VI. Mater Sci Eng A 2000;A280:30.
[32] Zakharov VV. Metal Sci Heat Treat 1997;39:61.
[33] Zakharov VV, Rostova TD. Met Sci Heat Treat 2007;49:435.
[34] Kharakterova ML, Eskin DG, Toropova LS. Acta Metall Mater 1994;42:2285.
[35] Du G, Deng J, Wang Y, Yan D, Rong L. Scr Mater 2009;61:532.
[36] Wolverton C. Acta Mater 2007;55:5867.
[37] Simonovic D, Sluiter MHF. Phys Rev B 2009;79:054304.
[38] Knipling KE, Dunand DC, Seidman DN. Acta Mater 2011;59:943.
[39] Booth-Morrison C, Dunand DC, Seidman DN. Acta Mater 2011;59:7029.
[40] Booth-Morrison C, Seidman DN, Dunand DC. Acta Mater 2012;60:3643.
[41] Ozolins V, Sadigh B, Asta M. J Phys Condens Matter 2005;17:2197.
[42] Asta M, Ozolins V, Woodward C. JOM 2001;53:16.
[43] Asta M, Ozolins V. Phys Rev B 2001:6409.
[44] Asta MN, Ozolins V, Hoyt JJ, van Schilfgaarde M. Phys Rev B 2001:6402.
[45] Clouet E, Sanchez JM, Sigli C. Phys Rev B: Condens Matter Mater Phys 2002;65:094105/1.
[46] Ghosh G, Asta M. Acta Mater 2005;53:3225.
[47] Ghosh G, van de Walle A, Asta M. Acta Mater 2008;56:3202.
[48] Ozolins V, Asta M. Phys Rev Lett 2001;86:448.
[49] Asta M, Foiles SM, Quong AA. Phys Rev B 1998;57:11265.
[50] Sandberg N, Holmestad R. Phys Rev B 2006;73:014108.
[51] Mantina M, Wang Y, Arroyave L, Chen Q, Liu ZK, Wolverton C. Phys Rev Lett 2008;100:215901.
[52] Bajikar SS, Larson DJ, Kelly TF, Camus PP. Ultramicroscopy 1996;65:119.
[53] Kelly TF, Camus PP, Larson DJ, Holzman LM, Bajikar SS. Ultramicroscopy 1996;62:29.
[54] Kelly TF, Larson DJ. Mater Charact 2000;44:59.
[55] Seidman DN. Rev Sci Instrum 2007;78:030901/1.
[56] Bunton JH, Olson JD, Lenz DR, Kelly TF. Microsc Microanal 2007;13:418.
[57] Seidman DN. Annu Rev Mater Res 2007;37:127.
[58] Kelly TF, Miller MK. Rev Sci Instrum 2007;78:031101/1.
[59] Hellman OC, Vandenbroucke JA, Rusing J, Isheim D, Seidman DN. Microsc Microanal 2000;6:437.
[60] Hellman OC, Blatz du Rivage J, Seidman DN. Ultramicroscopy 2003;95:199.
[61] Miller MK, Kenik EA. Microsc Microanal 2004;10:336.
[62] Karnesky RA, Dunand DC, Seidman DN. Acta Mater 2009;57:4022.
[63] Knipling KE, Karnesky RA, Lee CP, Dunand DC, Seidman DN. Acta Mater 2010;58:5184.
[64] van Dalen ME, Dunand DC, Seidman DN. J Mater Sci 2006;41:78814.
[65] Krug ME, Werber A, Dunand DC, Seidman DN. Acta Mater 2009;58:134.
[66] Krug ME, Dunand DC, Seidman DN. Acta Mater 2011;59:1700.
[67] Parratt LG. Probability and experimental errors in science. New York: John Wiley; 1966.
[68] Marquis EA, Seidman DN, Asta M, Woodward C, Ozolins V. Phys Rev Lett 2003;91:036101.
[69] Sudbrack CK, Noebe RD, Seidman DN. Phys Rev B 2006;73:212101.
[70] Wu ZG, Cohen RE. Phys Rev B 2006;73.
[71] Kresse GJ. Non-Cryst Solids 1996;205–207:833.
[72] Kresse G, Furthmueller J. Phys Rev B: Condens Matter 1996;54:11169.
[73] Kresse G, Furthmuller J. Comp Mater Sci 1996;6:15.
[74] Kresse G, Hafner J. Phys Rev B: Condens Matter Mater Phys 1993;47:558.
[75] Kresse G, Hafner J. Phys Rev B: Condens Matter Mater Phys 1994;49:14251.
[76] Kresse G, Joubert D. Phys Rev B 1999;59:1758.
[77] Perdew JP, Burke K, Ernzerhof M. Phys Rev Lett 1996;77:3865.
[78] Tabor D. Brit J Appl Phys 1956;7:159.
[79] Zhang H, Wang S. Comput Mater Sci 2011;50:2162.
[80] Marquis EA, Seidman DN, Dunand DC. Acta Mater 2003;51:285.
[81] Fuller CB, Seidman DN, Dunand DC. Acta Mater 2003;51:4803.
[82] van Dalen ME, Seidman DN, Dunand DC. Acta Mater 2008;56:4369.
[83] Karnesky RA. PhD thesis. Evanston (IL): Northwestern University; 2007. p. 258.
[84] Karnesky RA, van Dalen ME, Dunand DC, Seidman DN. Scr Mater 2006;55:437.
[85] Mondolfo LF. Aluminum alloys: structure and properties. London: Butterworths; 1976.
[86] Triftshaeuser W. Phys Rev B 1975;12:4634.
[87] Berger AS, Ockers ST, Chason MK, Siegel RW. J Nucl Mater 1978;69–70:734.
[88] Fluss MJ, Smedskjaer LC, Chason MK, Legnini DG, Siegel RW. J Nucl Mater 1978;69–70:586.
[89] Lynn KG, Schultz PJ. Appl Phys 1985;A37:31.
[90] Asato M, Mizuno T, Hoshino T, Masuda-Jindo K, Kawakami K. Mater Sci Eng A 2001;A312:72.
[91] Hoshino T, Papanikolaou N, Zeller R, Dederichs PH, Asato M, Asada T, et al. Comput Mater Sci 1999;14:56.
[92] Polatoglou HM, Methfessel M, Scheffler M. Phys Rev B. 1993;48:1877.
[93] Terblans JJ. Surf Interface Anal 2003;35:548.

[94] Henkelman G, Uberuaga BP, Jonsson H. J Chem Phys 2000;113:9901.

[95] Fuller CB, Seidman DN. Acta Mater 2005;53:5415.

[96] Lefebvre W, Danoix F, Hallem H, Forbord B, Bostel A, Marthinsen K. J Alloys Compd 2009;470:107.

[97] Clouet E, Barbu A, Lae L, Martin G. Acta Mater 2005;53:2313.

[98] Hallem H, Lefebvre W, Forbord B, Danoix F, Marthinsen K. Mater Sci Eng A 2006;A421:154.

[99] Ardell AJ. Metall Trans A 1985;16A:2131.

[100] Argon A. Strengthening mechanisms in crystal plasticity. Oxford: Oxford University Press; 2007.

[101] Meyers M, Chawla K. Mechanical metallurgy: principles and applications. Englewood Cliffs (NJ): Prentice-Hall; 1984.

[102] Frost H, Ashby M. Deformation mechanism maps. Oxford: Pergamon Press; 1982.

[103] Fu C. J Mater Res 1990;5:971.

[104] George E, Pope D, Fu C, Schneibel J. ISIJ Intern 1991;31:1063.

[105] Fukunaga K, Shouji T, Miura Y. Mater Sci Eng 1997;A239:202.

[106] Hyland R, Stiffler R. Scripta Metall Mater 1991;25:473.

[107] Nembach E. Particle strengthening of metals and alloys. New York: John Wiley; 1997.